J Adv Ceram

Research Article

Achieving a large field-induced polarization and energy density in $BaTiO_3$ films sputter-deposited on Si at 200 °C via a buffer-layer technique

Chao Liu[1], Jun Ouyang[1,2,3,✉], Yuyao Zhao[3], Hanfei Zhu[1], Hongbu Cheng[1], Zhenyan Liang[1], Li Wang[1]

Cite this article: Liu C, Ouyang J, Zhao Y, et al. *J Adv Ceram* 2025, **14**(3): 9221038. https://doi.org/10.26599/JAC.2025.9221038

ABSTRACT: Ferroelectric oxide films with a large field-induced polarization can be used in dielectric capacitors for charge or energy storage in microelectronic systems and hence have attracted intense research interest. A high processing temperature is usually required to produce a well-crystallized polar phase and hence a large polarization in the film, corresponding to a high charge or energy density. However, high processing temperature not only reduces the charge–discharge efficiency by producing a sizable remnant polarization but is also incompatible with the integration process. In this study, we address this problem by creating a large field-induced polarization (~55.8 μC/cm²) in $BaTiO_3$ films sputter-deposited on Si at 200 °C via a buffer-layer technique. This large polarization led to a high energy density and efficiency (W_{rec} ≈ 94.7 J/cm³, η ≈ 78.2%@4 MV/cm). The thickness of $LaNiO_3$ buffer layer was revealed to be the key factor determining the electric polarization (remnant and field-induced ones). A 50 nm $LaNiO_3$ thickness, corresponding to the aforementioned polarization and energy storage performance, not only ensures proper crystallization in the $BaTiO_3$ film, but also leads to an optimal combination of polycrystalline grains with a high dielectric constant. The latter accounts for the majority of the field-induced polarization. Our results revealed the key role of a buffer layer in tuning the microstructure of a low-temperature deposited ferroelectric oxide film. Furthermore, the excellent charge/energy storage performance of these 200 °C-deposited $BaTiO_3$ films has provided many opportunities for this simple dielectric in microelectronics.

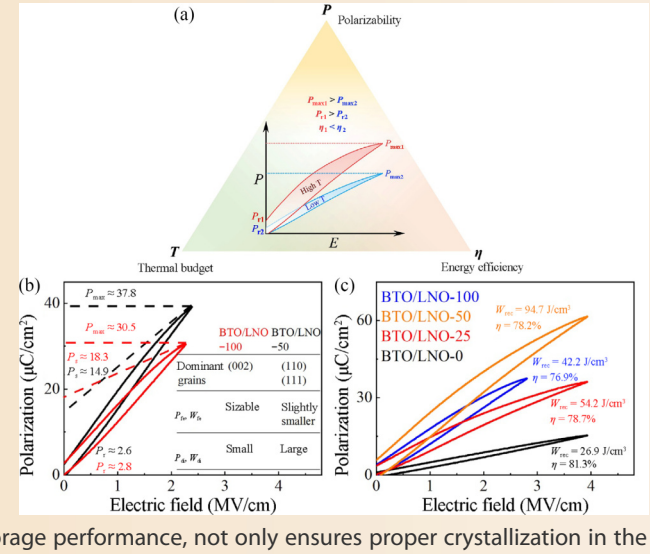

KEYWORDS: ferroelectric oxide films; field-induced polarization; $BaTiO_3$; $LaNiO_3$; energy density

1 Introduction

Recently, dielectric energy storage using ferroelectric ceramic capacitors has become a research frontier because of the combination of high power density, superior thermal stability and high cycling capability in such electrical devices. Among various ferroelectric ceramics, perovskite ferroelectrics such as $BaTiO_3$ [1–3] and $Pb(Zr,Ti)O_3$ [4–6] have been the most investigated. This can be attributed to their large ferroelectric polarizations, high dielectric constants, and a rich knowledge base formed during previous studies. This knowledge base covers single-component [7] and composite materials [8], as well as devices [9]. The integration of perovskite ferroelectrics on Si was explored long before the upsurge of research interest in dielectric energy storage. Non-volatile ferroelectric random-access memory (NVFeRAM) [10–12] and piezoelectric micro-electro–mechanical system (Piezo-MEMS) [13–15] are two major technological drives for the development of Si-based perovskite ferroelectric films. These early integration attempts have revealed that the high processing temperature, used to achieve good crystallization in the film, enables the film to display long-range ordered ferroelectricity, i.e., a parallelogram-shaped polarization–electric

[1] Institute of Advanced Energy Materials and Chemistry, Jinan Engineering Laboratory for Multi-scale Functional Materials, Shandong Provincial Key Laboratory of Molecular Engineering, School of Chemistry and Chemical Engineering, Qilu University of Technology (Shandong Academy of Sciences), Jinan 250353, China. [2] Key Laboratory of Key Film Materials & Application for Equipments (Hunan Province), Hunan Provincial Key Laboratory of Thin Film Materials and Devices, School of Material Sciences and Engineering, Xiangtan University, Xiangtan 411105, China. [3] Key Laboratory for Liquid–Solid Structure Evolution and Processing of Materials (Ministry of Education), School of Materials Science and Engineering, Shandong University, Jinan 250061, China.

✉ Corresponding author. E-mail: ouyangjun@qlu.edu.cn

Received: December 5, 2024; Revised: January 15, 2025; Accepted: January 17, 2025

field (*P*–*E*) hysteresis loop. Such a *P*–*E* loop is believed to be the key for realizing the traditional functional properties of a ferroelectric film, such as data storage [10–12] and piezoelectric sensing/actuating properties [13–15]. However, with the rapid development of new applications, including high dielectric constant (high-*k*) charge storage capacitors or gate layers [16,17] and high-density energy storage capacitors [18–23], "reverse engineering" of the ferroelectric behavior, i.e., the *P*–*E* loop, has gained broad interest among researchers of ferroelectric ceramics and films. This method aims at creating a large field-induced polarization while minimizing the remnant polarization, eventually creating a pseudo-linear *P*–*E* loop with a significantly reduced hysteresis.

With the recent developments in power and energy buffering systems for microelectronics [24,25] and in integrated charge storage [16,17] or memory devices [26–28], the call for thin-film perovskite ferroelectrics with a reversely engineered *P*–*E* loop has arisen among the material scientists in electroceramics. A trilemma between thermal budget, polarizability, and energy efficiency has emerged for ferroelectric films (Fig. 1). A low substrate temperature during deposition is desirable for seamless integration of ferroelectric films into current and future microelectronics (preventing the proliferation of thermal defects, e.g., those due to accelerated inter-diffusion at a high temperature). However, this low-temperature process inevitably leads to poor crystallization and weakened polarizability (small electric polarization and dielectric constant) of the film. On the other hand, well-crystallized films do show a high polarizability, but at the same time, the remnant electric polarization, a measure of how difficult a ferroelectric can be depolarized/discharged by the withdrawal of an applied electric field, increases with improved polarizability/crystallinity, leading to a low energy efficiency of the ferroelectric film capacitor. In this work, we propose a solution to this trilemma by using a simple prototype perovskite $BaTiO_3$.

As a lead-free perovskite ferroelectric, eco-friendly barium titanate $BaTiO_3$ (BTO) has gained intensive research attention in the last few decades because of its excellent dielectric, ferroelectric and piezoelectric properties [7–9,11,15]. It has been widely used in electronic and electro-optic film devices, such as capacitors [9,29,30], sensors [3,31,32], memories [8], and resonators [33,34]. The efforts in lowering the processing temperature of BTO films dated back to 1996, when Chang *et al.* [35] sputter-deposited BTO films on p-Si substrates at 500 °C and studied the performance and stability of Au/BTO/Si (metal–ferroelectric–semiconductor) capacitors. Later, in 2002, Law *et al.* [36] prepared BTO films via

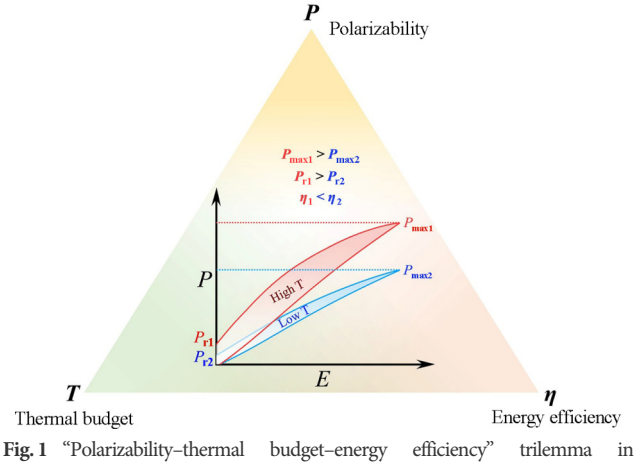

Fig. 1 "Polarizability–thermal budget–energy efficiency" trilemma in preparation of integratable high energy density ferroelectric film capacitors.

the sol–gel method, which resulted in a dielectric constant of ~26 at a processing temperature of 300 °C. A year later, Wen *et al.* [37] reported a polycrystalline perovskite phase in sol–gel-deposited BTO films via a hydrothermal process at 200 °C. A dielectric constant of ~20 was achieved in such films with a thickness of approximately 500 nm. Nam *et al.* [38] prepared thick BTO films via aerosol deposition in 2004, which showed a dielectric constant of ~140 after being annealed at 300 °C for 2 h. Zhu *et al.* [39] prepared $BaTiO_3$ films on $LaAlO_3$ substrates via molecular beam epitaxy (MBE) in 2006, and they discovered a novel approach to prepare a buffer layer of BTO consisting of 8 monolayers with a decreasing deposition temperature from 600 to 300 °C. This BTO buffer layer promotes the growth of crystalline BTO films at temperatures as low as 280 °C. In 2009, Xu *et al.* [40] prepared highly (001)-oriented BTO films via a sol–gel–hydrothermal process in combination with a buffer layer technique. When the annealing temperature was set at 400 °C, the BTO film exhibited a high dielectric constant ($\varepsilon_r \approx 276@E \approx 0$) and a small remnant polarization ($P_r \approx 2.5$ μC/cm^2). However, the field-induced polarization was also small and saturated at a small electric field (~10 μC/cm^2@E = 0.3 MV/cm). These hydrothermally processed BTO films also showed relatively high dielectric losses due to residual functional groups.

In our previous investigations, we used industrially scalable radio frequency (RF) sputtering as the deposition technique, for the preparation of BTO films with a low thermal budget to be compatible with the complementary metal oxide semiconductor (CMOS)-Si process ($T \leq 500$ °C) [41–47]. We started with the deposition of BTO films directly on the platinized Si substrates [44]. Later, the optimized BTO films with a submicron thickness grown on Pt/Ti/(100)Si substrates at 500 °C showed a high field-induced polarization (P_{fi}) of ~40–50 μC/cm^2 at ~3 MV/cm, while 1–2 μm thick films showed a higher P_{fi} of ~55–65 μC/cm^2 at ~2 MV/cm [45]. However, owing to their large grain size, the remnant polarizations of these films are sizable (~10–15 μC/cm^2), and the breakdown fields are not high, leading to mediocre energy storage densities and low charge–discharge efficiencies (η). On the other hand, by using a buffer layer of $LaNiO_3$ (LNO), which promoted the (001)-textured growth of BTO, we not only maintained a high field-induced polarization in BTO films deposited at 500 °C [45,46] but also increased their breakdown fields E_b by reducing the average grain size. Consequently, higher charge and energy storage densities were achieved in these LNO-buffered BTO films. BTO films deposited at even lower temperatures (~350–400 °C) with a LNO buffer layer are still well crystallized with smaller grains, resulting in better overall energy storage performance (higher E_b, smaller P_r and higher η)[43,47]. A record-high capacitive energy density on Si of ~229 J/cm^3 with an energy efficiency of ~69.2% (at 8.75 MV/cm) was achieved in BTO films deposited on LNO-buffered platinized Si at 350 °C, with the thicknesses of the BTO and LNO layers being optimized to achieve a small grain size and a desirable compressive residual strain [47]. In this case, the field-induced polarization is as high as ~75 μC/cm^2 at ~8.75 MV/cm. Overall, the sputter-deposited BTO films are compatible with the CMOS-Si process, with high charge and energy densities desirable for integrated capacitor applications.

In this work, we successfully pushed the low-temperature threshold for deposition of ferroelectric BTO films down to 200 °C, an achievement desirable for the future development of microelectronics. Furthermore, we demonstrated that the charge and energy storage performances of BTO films can be optimized by engineering the buffer layer thickness. The use of a LNO buffer layer with an intermediate thickness of ~50 nm resulted in a

large field-induced polarization (~55.8 μC/cm²@4 MV/cm) and a high energy density and efficiency (W_{rec} ≈ 94.7 J/cm³, η ≈ 78.2%@4 MV/cm).

2 Methods and characterizations

$BaTiO_3$ films were deposited by using the RF-magnetron sputtering technique. The vacuum chamber was pumped down to a base pressure of 2×10^{-4} Pa prior to film deposition. Next, a bottom electrode layer (Pt/Ti), a $LaNiO_3$ buffer layer (0, 25, 50, and 100 nm), and a ferroelectric $BaTiO_3$ film (thickness targeted at 300 nm) were consecutively deposited on a SiO_2/(100)Si substrate (length × width × thickness: 10 mm × 10 mm × 0.5 mm) from corresponding metallic or ceramic targets with a 2-inch diameter. The platinized Si substrate, i.e., Pt/Ti/SiO_2/(100)Si, is also commercially available. The metallic targets were purchased from Zhongnuo Advanced Material Technology Co., Ltd., China, with 99.99% (4N) purity, while the ceramic targets were provided by the Anhui Institute of Optics, Chinese Academy of Sciences, China, with 99.9% (3N) purity. The deposition parameters are summarized in Table 1. Notably, owing to a reduced substrate temperature, shorter target-substrate distances were used to promote nucleation and growth of the ceramic layers. Notably, the compatibility temperature (highest temperature) of the whole deposition process is 300 °C, which is the deposition temperature of Pt/Ti electrode.

The information on phase structures and crystalline orientations of the thin film heterostructures was collected via normal X-ray diffraction (XRD) 2θ-scans and grazing incidence X-ray diffraction (GIXD) (parallel beam, incidence angle of 0.4°) 2θ-scans (Rigaku Dmax-2500PC, equipped with a Ni-filtered Cu-Kα radiation source, Rigaku, Japan). The surface morphology of the BTO films was analyzed via an atomic force microscope (AFM; Cypher ES SPM, Oxford Instruments, UK), using an AD-2.8-SS scanning probe (tip curvature radius r < 5 nm, Adama Innovations, Ireland). The cross-sectional morphology, nanostructure, and elemental composition of the BTO/LNO/Pt/Ti thin film heterostructures were investigated via a transmission electron microscope (TEM; JEM-2010, JEOL, Japan, equipped with an energy dispersive spectrometer (EDS)). For electrical measurements, circular Au top electrodes (with a diameter of 200 μm and a thickness of approximately 100 nm) were sputtered onto the BTO films at room temperature with the aid of a shadow mask. The pseudo-static ferroelectric hysteresis (50–5000 Hz) and polarization fatigue behavior of the BTO films were measured by using a ferroelectric tester (Precision Premier II, Radiant Technology, USA). The frequency-dependent dielectric properties were obtained from small-field capacitance–frequency tests (ε_r–f/tgδ–f) by using a high-precision LCR meter (Quad-Tech 7600 plus, Chroma Systems Solutions, USA).

3 Results and discussion

The XRD and GIXD 2θ-scan patterns of the BTO/LNO/Pt/Ti thin film heterostructures deposited on SiO_2/(100)Si are displayed in Fig. 2(a) and 2(b), respectively. BTO films with different thicknesses of the LNO buffer layer (0, 25, 50, and 100 nm) were named BTO/LNO-0, BTO/LNO-25, BTO/LNO-50, and BTO/LNO-100. Figure 2(a) shows that the BTO/LNO-0 and BTO/LNO-25 films were poorly crystallized, which can be attributed to a zero or weak buffering effect with a diminishing LNO thickness. On the other hand, the BTO/LNO-50 and BTO/LNO-100 films clearly presented diffraction peaks corresponding to the perovskite LNO and BTO, indicating successful buffered growth of crystalline films on platinized Si.

To better analyze the crystalline orientations and estimate the relative volume fractions of the grains in the crystalline phase, GIXD 2θ-scans were carried out in a 2θ range between 25° and 50°, which revealed the existence of (110)-, (111)- and (002)-oriented grains in all the films. Fittings of these diffraction peaks were carried out using the Lorentzian function. Furthermore, the volume fraction of grains with a certain crystalline orientation was estimated by using its orientation degree [48], i.e., the areal integral of its fitted peak weighted over the sum of areal integrals of the fitted peaks for all grains. For example, the volume fraction of the (002) grains is estimated according to

Table 1 Sputter-deposition parameters of BTO/LNO/Pt/Ti thin film heterostructures

Layer	Ti	Pt	LNO	BTO
Deposition temperature (°C)	300	300	200	200
Deposition atmosphere (mL/min)	Ar, 39	Ar, 39	Ar, 60; O_2, 15	Ar, 60; O_2, 15
Target–substrate distance (cm)	5	5	4.5	4
Deposition power (W)	55	55	100	100
Deposition time (min)	5	15	0, 5, 10, 20	80
Deposition pressure (Pa)	0.3	0.3	0.3	1.2

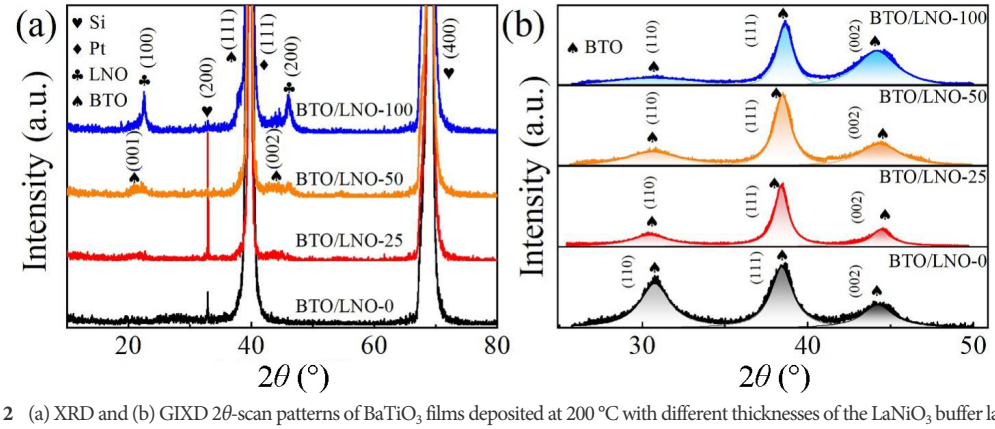

Fig. 2 (a) XRD and (b) GIXD 2θ-scan patterns of $BaTiO_3$ films deposited at 200 °C with different thicknesses of the $LaNiO_3$ buffer layer.

$\alpha_{(002)} = I_{(002)}/(I_{(002)} + I_{(110)} + I_{(111)})$. The estimated volume fractions of the (002), (110), and (111) grains in the crystalline phase are listed in Table 2 for the four BTO films. As the LNO thickness was increased, the dominant grain orientation(s) evolved from (110) and (111) in BTO/LNO-0 to (111) in BTO/LNO-25 and BTO/LNO-50 and finally to (002) in BTO/LNO-100.

This orientation evolution can be attributed to the competing effects between a buffering (111) Pt electrode, which promotes (111) BTO grain growth [44], and a buffering (100)-textured LNO layer, which promotes the (001) BTO grain growth [43,45–47], and lastly the natural tendency of BTO grain growth along its most densely packed plane [44], i.e., (110) for perovskite films. The dielectric properties of the BTO films, therefore, are highly dependent on the thickness of the LNO layer. This is due not only to improved crystallinity with an increasing buffer layer thickness, but also to the orientation-dependent ferroelectric polarization and dielectric constant. Although showing a lower ferroelectric polarization in tetragonal $BaTiO_3$ than in the (001) polar orientation, the non-polar orientations of (111) and (110) have shown much higher dielectric constants than that of the (001) orientation [49], making it possible to optimize the overall polarization response with both ferroelectric and linear dielectric contributions [50]. Notably, except for the BTO/LNO-100 film, all the other films showed a dominant grain population in non-polar orientations, i.e., 70%–80% of their grains are (111)/(110). However, the overall polarization response also depends on the degree of crystallinity, which will be re-evaluated via TEM analyses.

The cross-sectional film morphology and nanostructures of the BTO films were analyzed via TEM. Representative low-resolution cross-sectional TEM images of the three LNO-buffered BTO films are displayed in Figs. 3(a)–3(c). First, all the BTO films showed a dense columnar nanograin morphology, which was induced by the underlying LNO buffer layer, as can be visualized by their interconnected grains (especially in Fig. 3(c)). The thicker the LNO buffer layer is, the denser the BTO nanograins are packed, i.e., the crystallinity of the BTO film improves with an increasing LNO layer thickness. Notably, these BTO nanograins did not follow a continuous growth pattern, as reported previously for those grown at 350 °C or a higher temperature [43]. This is due to a greater degree of "undercooling" (the temperature difference between the substrate and vapor phase) [43], which has led to repeated nucleation throughout the film growth process, resulting in a tilted and broken columnar nanograin morphology. The clean-cut interfaces between BTO and LNO, as well as those between LNO and Pt/Ti, Pt/Ti and SiO_2, indicate smooth and uniform growth of these thin film heterostructures. The thickness (~150 nm) and grain morphology of the Pt electrode layer are approximately the same for the three thin film heterostructures, so are the thicknesses of the BTO films (~300±50 nm). Therefore, the crystalline nanostructures of the BTO films are determined mostly by the LNO buffer layer. In Figs. 3(a)–3(c), an initial amorphous LNO layer of ~10 nm thickness was observed in all

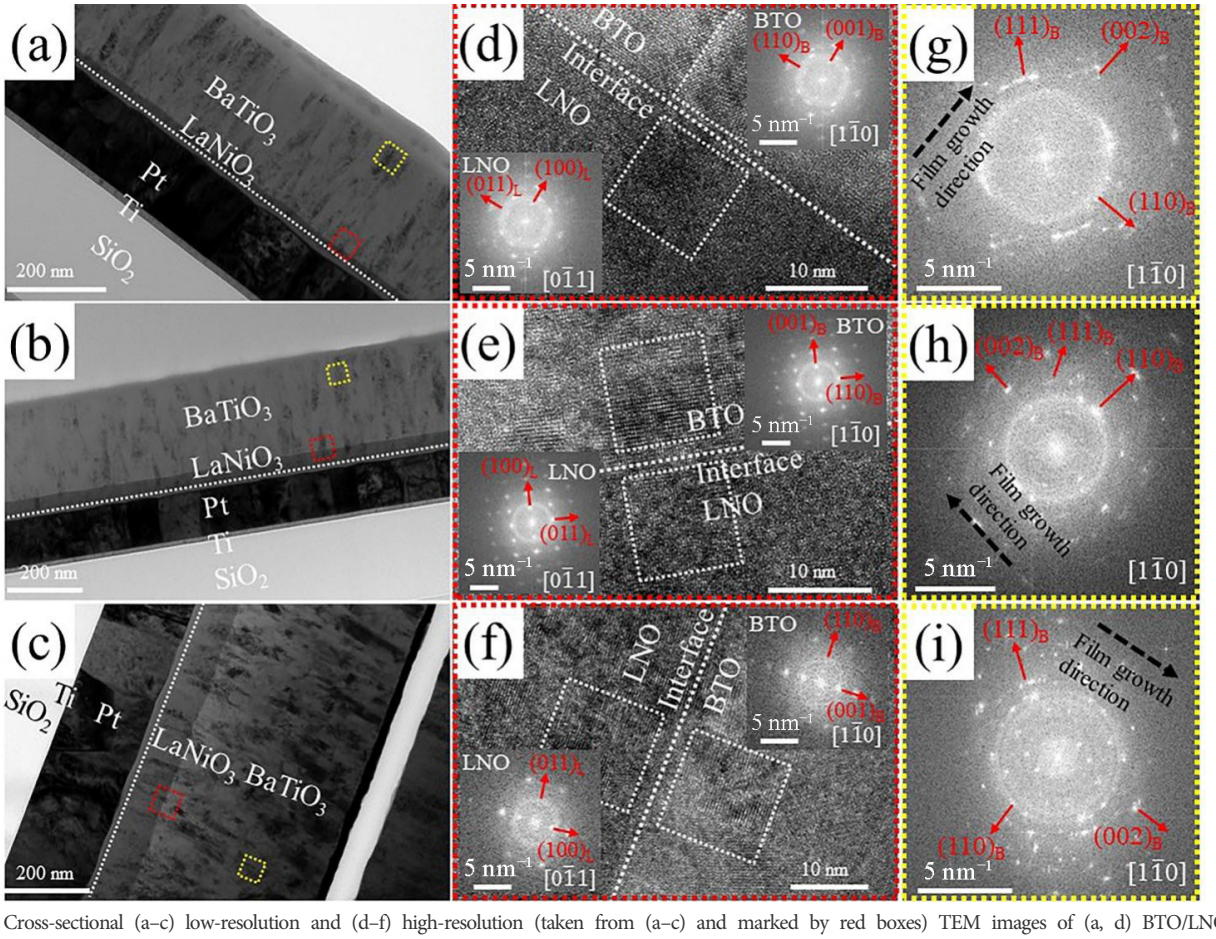

Fig. 3 Cross-sectional (a–c) low-resolution and (d–f) high-resolution (taken from (a–c) and marked by red boxes) TEM images of (a, d) BTO/LNO-25, (b, e) BTO/LNO-50, and (c, f) BTO/LNO-100 bi-layer films grown on Pt/Ti/SiO_2/(100)Si. The insets in (d–f) and (g–i) are FFT-SAED patterns taken from near BTO/LNO interface (insets in (d–f)) and film surface ((g–i) marked by yellow boxes in (a–c)). The zone axis is [1̄10] for (d–i) all ED patterns. Subscripts L and B denote LNO and BTO, respectively.

three thin film heterostructures (its interface with the crystalline LNO region is marked by a white dashed line). This is consistent with the low substrate temperature at 200 °C. Such an amorphous layer will deter the consequent nucleation and growth of perovskite BTO grains [51], and its effect strengthens with a reducing total thickness of LNO.

As shown in Figs. 3(d)–3(f), high-resolution TEM (HRTEM) images were taken from the interfacial regions of BTO/LNO-25, BTO/LNO-50 and BTO/LNO-100 bi-layer films (marked by red boxes in Figs. 3(a)–3(c)), respectively. The improved crystallinity of the bi-layer film with an increasing LNO thickness can be clearly observed from these HRTEM images. As shown in Fig. 3(d), the lattice fringes in both LNO and BTO layers are discontinuous and surrounded by an amorphous matrix, indicating a low degree of crystallinity in BTO/LNO-25. The SAED patterns taken from the two layers display the coexistence of a non-crystalline phase (diffused ring pattern) and a textured perovskite phase of $(100)_{LNO}$ and $(001)_{BTO}$. The growth relationship is $(100)_{LNO}//(001)_{BTO}$ with $[100]_{LNO}//[001]_{BTO}$ and $[011]_{LNO}//[110]_{BTO}$, which is as expected because of the close lattice matching between the two perovskite oxides. As the thickness of the LNO layer was increased to 50 and 100 nm, the lattice fringes became continuous and dominant in the HRTEM images as shown in Fig. 3(e) and 3(f), indicating a high degree of crystallization. The SAED patterns for LNO and BTO layers displayed dominant textured perovskite phases of $(100)_{LNO}$ and $(001)_{BTO}$, with the same growth relationship as that shown in Fig. 3(d). In addition, there was a minority population of non-crystalline phases in both layers, as revealed by the diffused ring patterns superimposed on the diffraction patterns of $(100)_{LNO}$ and $(001)_{BTO}$. The amorphous phase almost disappeared in the BTO/LNO-100 heterojunction, as evidenced by the weak diffused ring patterns in Fig. 3(f). These observations clearly indicate a (100) texture in the LNO buffer layer, which promoted a (001) textured growth in the BTO film near the BTO/LNO interface. The degree of crystallinity was improved with an increasing LNO thickness, and the BTO/LNO-50 and BTO/LNO-100 films were well crystallized.

Figures 3(g)–3(i) display fast-Fourier transformed selected area electron diffraction (FFT-SAED) patterns for the local BTO film away from the BTO/LNO interface in the BTO/LNO-25, BTO/LNO-50 and BTO/LNO-100 films, respectively. The BTO/LNO-25 film exhibited superimposed diffraction patterns consisting of weak $(002)_{BTO}$ along the film normal and strong diffraction rings of (110) and (111), indicating its inclusion of all three major grains and the dominance of the latter two. Moreover, the BTO/LNO-50 film showed strong diffraction ring patterns of (110) and (111), supplemented by an enhanced $(002)_{BTO}$ along the film normal. Finally, the BTO/LNO-100 film displayed a dominant $(002)_{BTO}$ ED pattern along the film normal (Fig. 3(i)), together with weak diffraction rings of (110) and (111). These observations are consistent with the results of GIXD analysis (Table 2). Overall, the BTO/LNO-50 and BTO/LNO-100 films displayed considerably higher levels of crystallinity, which is evidenced by the presence of brighter and sharper diffraction spots and rings in their respective SAED patterns.

EDS analysis was carried out to investigate the elemental

Table 2 Estimated volume fractions of (002), (110), and (111) grains in the crystalline phase of the $BaTiO_3$ films with different thicknesses of the $LaNiO_3$ buffer layer

Orientation\film	BTO/ LNO-0	BTO/ LNO-25	BTO/ LNO-50	BTO/ LNO-100
110	0.389	0.287	0.266	0.154
111	0.402	0.498	0.438	0.379
002	0.209	0.215	0.296	0.467

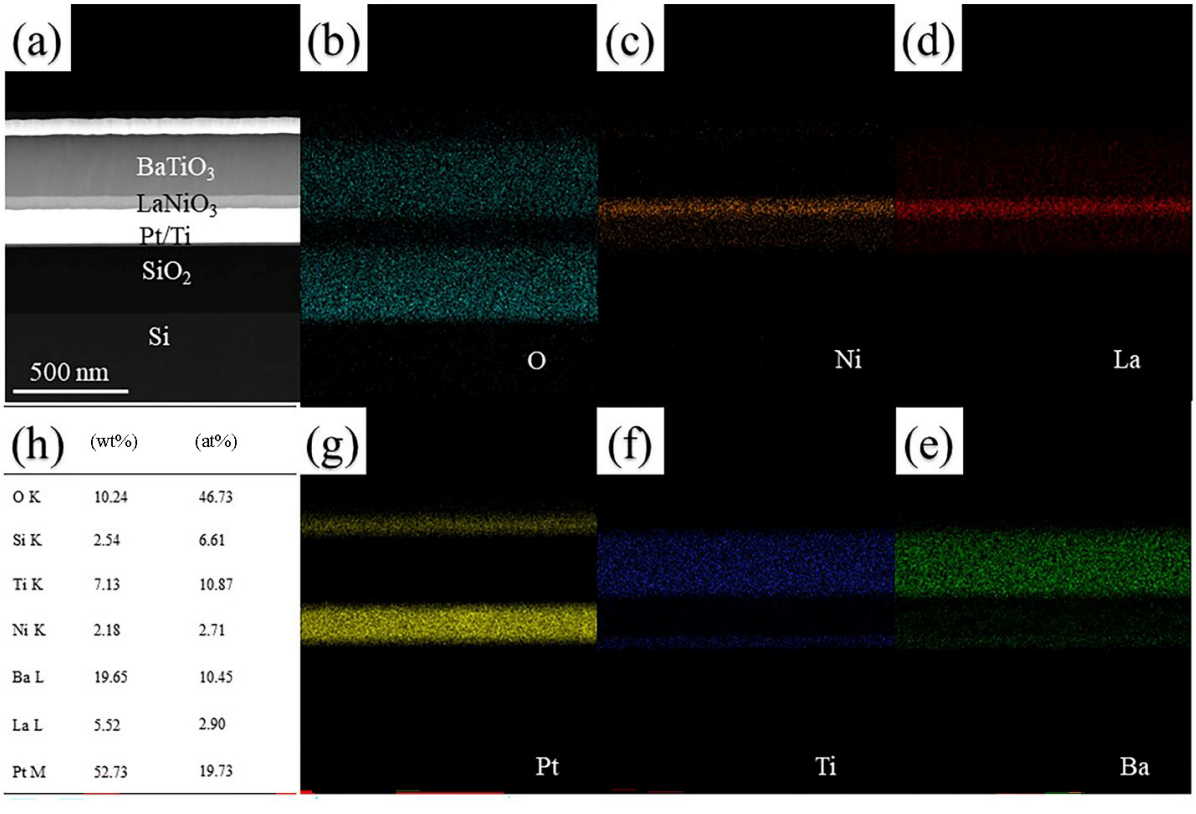

Fig. 4 (a) Low-magnification cross-sectional TEM image of BTO/LNO-50 film and (b–g) EDS elemental plane-scan profiles; (h) EDS elemental composition analysis.

composition of the BTO thin film heterostructures. Figures 4(b)–4(g) show the EDS elemental scan profiles of BTO/LNO-50 film on its cross-sectional plane (Fig. 4(a)), while Fig. 4(h) gives the elemental compositions. A chemically stoichiometric $BaTiO_3$ film was revealed, and the cross-sectional elemental scan profiles correlated well with the layered structure (the cap layer used for FIB preparation of the TEM sample was Pt). There was no severe interdiffusion of the constituent elements, which is an advantage of low-temperature processing [47]. Notably, Ba and Ti elements have very close EDS peaks, and in this case, the Ba "footprints" in the bottom half of Fig. 4(e) are actually from Ti (Fig. 4(f)).

The surface morphology of the LNO-buffered BTO films was investigated via AFM, and the results are shown in Fig. 5. A smooth surface with a fine-grained morphology was observed for all the films. The root-mean-square surface roughness values were 1.39, 1.96, and 1.93 nm for BTO/LNO-25, BTO/LNO-50, and BTO/LNO-100 films, respectively. Furthermore, the average surface grain size of the BTO films increased with an increasing buffer layer thickness, which was approximately 20.56, 28.72, and 30.15 nm for the three BTO films, respectively. These results are consistent with the estimated grain sizes from the TEM images (Figs. 3(a)–3(c)). The insets of Figs. 5(a)–5(c) present statistical analyses of the surface grain size, which were obtained by using the Nano Measurer™ software (Fudan University, China).

The polarization–electric field (*P*–*E*) hysteresis loops of these BTO films were measured at 1 kHz with an increasing maximum electric field until the *P*–*E* loop became leakage-dominant. The *P*–*E* loops are shown in Fig. 6, and the insets are the corresponding half *P*–*E* loops, which are used to simulate the charge–discharge process and evaluate the energy storage performance. Both the remnant (P_r) and field-induced polarization (P_{fi}) increased as the LNO thickness was increased from 0 to 50 nm. The BTO/LNO-0 film showed an unsaturated, pseudo-linear *P*–*E* loop with the smallest P_r (~1.0 μC/cm²) and P_{fi} (~14.4 μC/cm²) at E_{max} = 4 MV/cm, indicating a weak or zero ferroelectricity. This is consistent with its poor crystallinity, as revealed by the XRD analysis (Fig. 2(a)). On the other hand, when the LNO layer thickness was increased to 25 and 50 nm, P_r/P_{fi} increased and reached 3.8/32.4 and 5.9/55.8 μC/cm², respectively, under the same maximum electric field (E_{max} = 4 MV/cm). The *P*–*E* loops now became typical ferroelectric ones, showing a saturation trend of the polarization at the high-field end. These

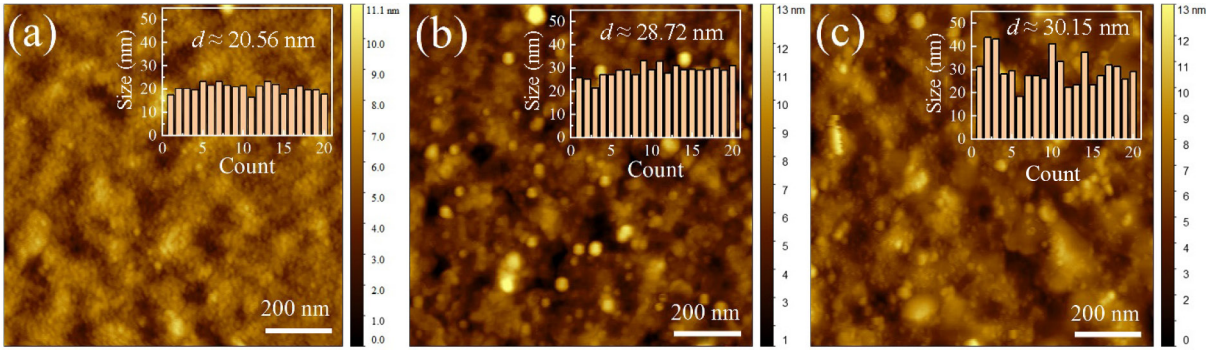

Fig. 5 (a–c) AFM surface scan images of BTO/LNO-25, BTO/LNO-50 and BTO/LNO-100 films, respectively, where the insets are the grain size distribution charts.

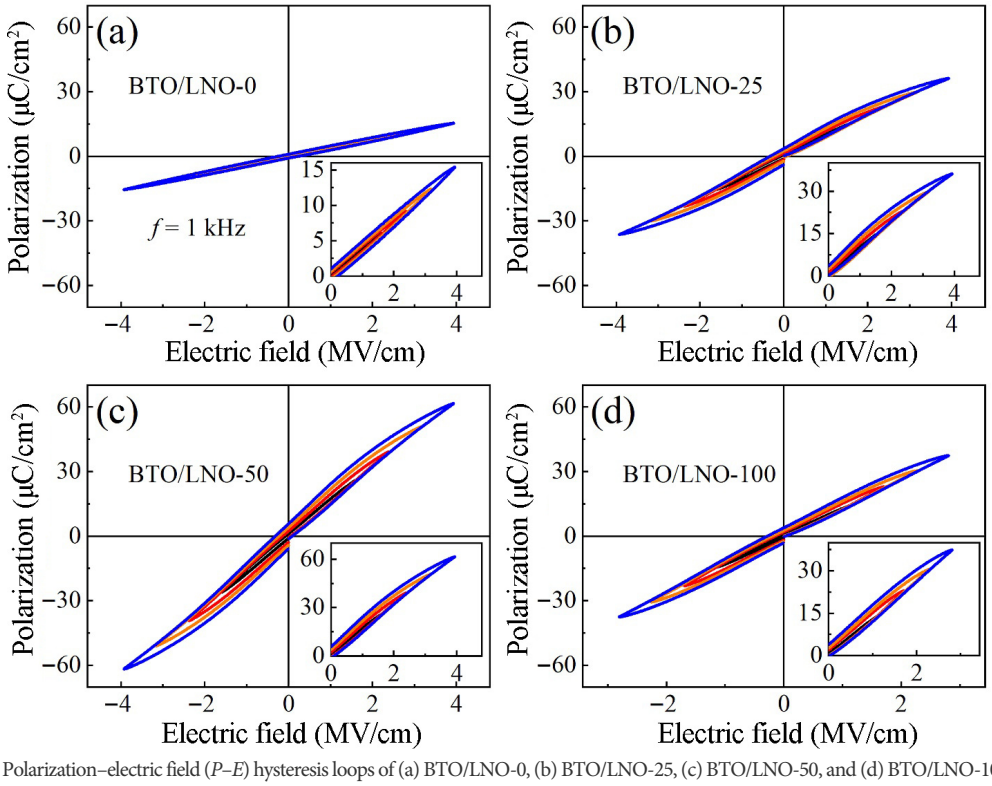

Fig. 6 Polarization–electric field (*P*–*E*) hysteresis loops of (a) BTO/LNO-0, (b) BTO/LNO-25, (c) BTO/LNO-50, and (d) BTO/LNO-100 films.

behaviors are consistent with the improved crystallinity of BTO films as a LNO buffer layer was added. However, a further increase in the LNO thickness of the BTO/LNO-100 film not only reduced its dielectric strength E_b (from 4 to 2.8 MV/cm), but also decreased the field-induced polarization P_{fi} compared with that of the BTO/LNO-50 film under the same electric field. This decrease in performance can be attributed to a change in the grain population, i.e., an increase in the (002) grain population at the cost of high dielectric constant grains of (110) and (111) [49]. While the reduced E_b in the BTO/LNO-100 film can be attributed to an early polarization saturation (Fig. 6(d)) due to a high degree of crystallization, as well as its larger and non-uniform grains (Fig. 5(c)), the energy storage performance needs to be further analyzed.

As shown in Fig. 7(a) and Table 3, we separated out the ferroelectric (P_{fe}, W_{fe}) and linear dielectric (P_{di}, W_{di}) contributions to the charge and energy storage performances by analyzing the half *P*–*E* loops of BTO/LNO-50 and BTO/LNO-100 at the same E_{max} (~2.2 MV/cm). The maximum polarizations (P_{max}) of the two films were 37.8 and 30.5 μC/cm² while their remnant polarizations (P_r) were 2.6 and 2.8 μC/cm², leading to field-induced polarizations (P_{fi}) of 35.2 μC/cm² (BTO/LNO-50) and 27.7 μC/cm² (BTO/LNO-100) ($P_{fi} = P_{max} - P_r$). The 7.5 μC/cm² increase in P_{fi} of the BTO/LNO-50 film came from its large (linear) dielectric contribution P_{di} ($P_{fi} = P_{di} + P_{fe}$, $P_{di} = P_{max} - P_s$), which shows an improvement of ~10.7 μC/cm² over that of the BTO/LNO-100 film (22.9 vs. 12.2 μC/cm²).

This advantage in the dielectric contribution overcompensated for its small disadvantage in the field-induced ferroelectric polarization P_{fe} ($P_{fe} = P_S - P_r$), which is ~3.2 μC/cm² smaller than that of the BTO/LNO-100 film (12.3 vs. 15.5 μC/cm²). Notably, the spontaneous polarizations P_S of the two films were obtained by extrapolating their *P*–*E* curves near saturation to the zero field, as shown in Fig. 7(a). The energy storage densities of the two films at 2.2 MV/cm, including the total recyclable energy density W_{rec} (due to P_{fi}) and its two components W_{fe} (due to P_{fe}) and W_{di} (due to P_{di}), followed the same trend as their corresponding polarizations. The BTO/LNO-50 film showed a recyclable energy density due to the linear dielectric response, i.e., W_{di}, approximately twice as large as that of the BTO/LNO-100 film (27.5 vs. 14.0 J/cm³), while for the ferroelectric component of W_{rec} (W_{fe}), the two films had a closely matched performance (13.1 vs. 14.9 J/cm³), with the latter slightly leading the way. From the above analysis, it can be concluded that the optimal charge and energy storage performances of the BTO/LNO-50 film are due to its large linear dielectric response, which is correlated with its grain population. Although having led to an enhanced ferroelectric contribution to the recyclable charge/energy density, the improved ferroelectricity in the (001)-dominant BTO/LNO-100 film resulted in early saturation of the ferroelectric

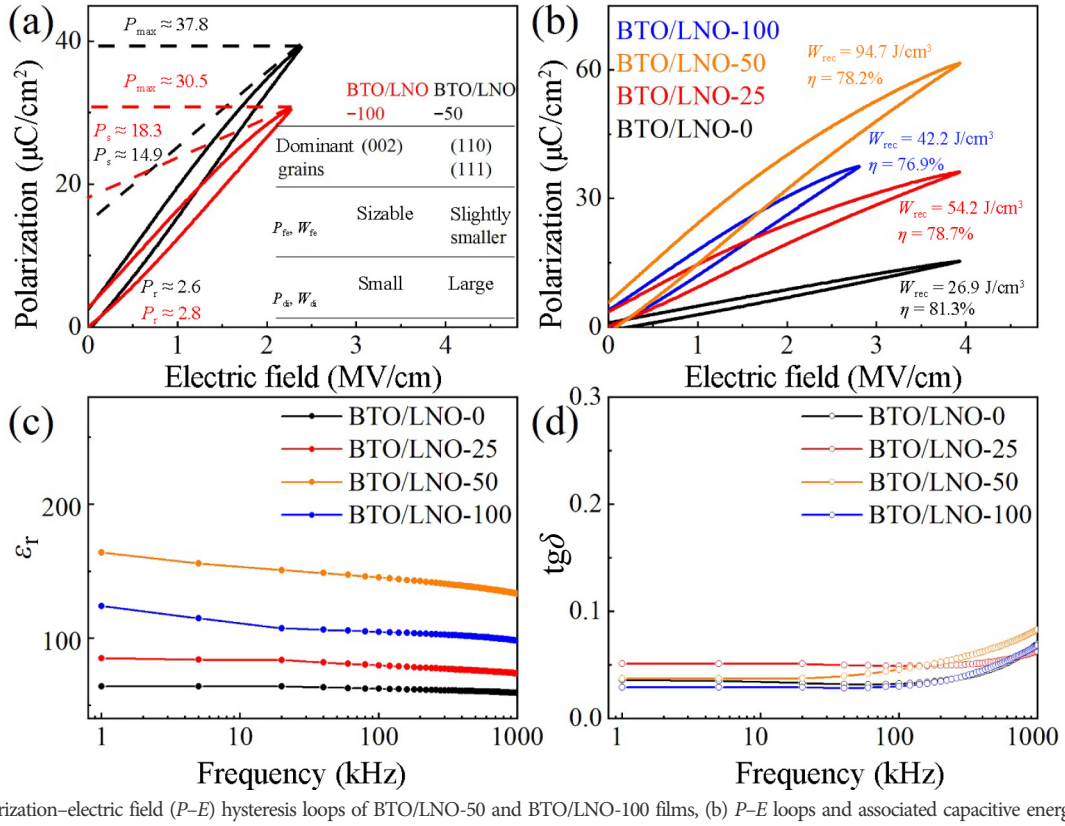

Fig. 7 (a) Polarization–electric field (*P*–*E*) hysteresis loops of BTO/LNO-50 and BTO/LNO-100 films, (b) *P*–*E* loops and associated capacitive energy densities and efficiencies, (c) dielectric constants, and (d) dielectric loss tangents as functions of the measuring frequency for the four BTO films.

Table 3 Polarizations and energy densities of BTO/LNO-50 and BTO/LNO-100 films at 2.2 MV/cm

Film	P_r	P_{max}	P_s	P_{fi} (= $P_{max} - P_r$)	P_{fe} (= $P_s - P_r$)	P_{di} (= $P_{max} - P_s$)	W_{rec} (due to P_{fi})	W_{fe} (due to P_{fe})	W_{di} (due to P_{di})
BTO/LNO-50	2.6	37.8	14.9	35.2	12.3	22.9	40.6	13.1	27.5
BTO/LNO-100	2.8	30.5	18.3	27.7	15.5	12.2	28.9	14.9	14.0

Note: the units for polarization charges (*P*) and energy densities (*W*) are μC/cm² and J/cm³, respectively.

polarization and hence a lower breakdown field. More importantly, its lack of high dielectric constant grains has led to a reduced linear dielectric response and hence small dielectric contributions to the field-induced polarization charge (P_{di}) and recyclable energy density (W_{di}). This is the main reason for its mediocre charge and energy storage performances, as detailed in Table 3.

As shown in Fig. 7(b), we put the half *P*–*E* loops of the four BTO films side by side, all at their corresponding maximum applicable fields. The recyclable energy storage density (W_{rec}) peaked at a LNO thickness of 50 nm (~94.7 J/cm^3), while the energy efficiency slightly decreased with an increasing LNO thickness. The BTO/LNO-100 film, with a smaller maximum applicable electric field at ~2.8 MV/cm, not only presented a mediocre W_{rec} of ~42.2 J/cm^3 but also the lowest energy efficiency η at ~76.9%. On the other hand, the BTO/LNO-50 film showed the highest W_{rec} together with a decent η of 78.2% under a large electric field of 4 MV/cm. Notably, such energy efficiency is among the highest reported for undoped $BaTiO_3$ films [43,46,47]. The dielectric constants (ε_r) and loss tangents (tgδ) as functions of the measuring frequency (f) of the four BTO films are displayed in Figs. 7(c) and 7(d), respectively. Similar to the polarization performance in Fig. 7(b), ε_r increased with an increasing LNO thickness until the latter reached 50 nm. At 1 kHz, ε_r was approximately 64 for BTO/LNO-0 and ~85 for BTO/LNO-25 and then reached a maximum at ~164 for BTO/LNO-50. A further increase in LNO thickness resulted in a reduced ε_r (~124) in BTO/LNO-100. These observations are consistent with the *P*–*E* results shown in Figs. 6, 7(a), and 7(b). Moreover, all the BTO films showed weak frequency dependence in their dielectric constants in the measuring frequency range of [1 kHz, 1 MHz], indicating insignificant polarization relaxations associated with the interface and bulk charge carriers [44]. Such ε_r–f curves have been observed in our low-temperature-sputtered ferroelectric oxide films [42,43,46], which contain a much reduced amount of thermally induced charged defects. Similarly, the dielectric losses of the BTO films are relatively low and flat with varying frequencies except near the high-frequency end. For example, the BTO/LNO-50 film has a tgδ of ~0.037 at 1 kHz, which increases to 0.046 at 100 kHz and finally to ~0.083 at 1 MHz. Thus, a large dielectric constant (comparable to those (001)-textured BTO films deposited at temperatures 150 to 200 °C higher [42,43,45,47,52]) and a low dielectric loss of the BTO/LNO-50 films, have ensured their excellent charge and energy storage performances with a good reliability against common capacitor failure modes (self-heating, thermal runaway, etc.) [53,54]. Finally, the electrical properties in Fig. 7 are well correlated with the results of the structural analyses in Fig. 2 through Fig. 5. To achieve optimal energy and charge storage performances in polycrystalline ferroelectric films, it is critical to find a delicate balance between crystallinity and grain orientation. Specifically, predeposition of a buffer layer promoted the growth of a crystalline BTO film at a low substrate temperature. However, too thick a buffer layer will lead to a high degree of crystallinity with a dominant (001) orientation, which not only results in an improved ferroelectricity with an early polarization saturation and dielectric breakdown, but also leads to a significantly reduced dielectric constant. Both of these consequences deteriorate the energy and charge storage performances of the film.

The frequency-dependent *P*–*E* loops of the BTO/LNO-50 film, measured at half of its maximum applicable electric field (2 MV/cm), are presented in Fig. 8(a) in the frequency range of 50–5000 Hz. Both the maximum (P_{max}) and remnant polarizations (P_r) increase with a decreasing measuring frequency, as is expected for the collection of polarization charges over an extended time period. Consequently, both the field-induced polarization (P_{fi}) and the recyclable energy density (W_{rec}) showed very small variations when changing the measuring frequency (inset of Fig. 8(a)). This observation reveals the good frequency stability of the charge/energy storage performance of the BTO/LNO-50 film. Moreover, the electric field cycling stability, i.e., fatigue resistance, of the BTO/LNO-50 film was investigated, and the results are shown in Fig. 8(b). After up to 10^9 times of bi-polar switching using an alternating current (AC) square wave of 500 kHz and a 2 MV/cm amplitude, the 1 kHz *P*–*E* loops measured after different cycling counts (1, 10^6, 10^7, 10^8, and 10^9) showed negligible differences, indicating an outstanding fatigue resistance. This finding is consistent with previous reports using a LNO buffer layer/buffered electrode [46,55].

Finally, Table 4 compares the dielectric energy storage performance of our polycrystalline $BaTiO_3$ films with those of the leading $BaTiO_3$ dielectric films [43,45–47,49,56–58]. In addition to the lowest processing temperature of 200 °C, our BTO film capacitors exhibit a strong overall performance including a large field-induced polarization (P_{fi}, 55.8 μC/cm^2), a large recyclable energy density (W_{rec}, 94.7 J/cm^3), and a high energy efficiency (η, 78.2%), all at a large fixed electric field of 4 MV/cm.

4 Conclusions

In summary, polycrystalline $BaTiO_3$ films were successfully sputter-grown on platinized Si (Pt/Ti/SiO_2/(100) Si) via a buffer layer technique at a low substrate temperature of 200 °C. Our results reveal the importance of the buffer layer thickness on the charge and energy storage performances of low-temperature

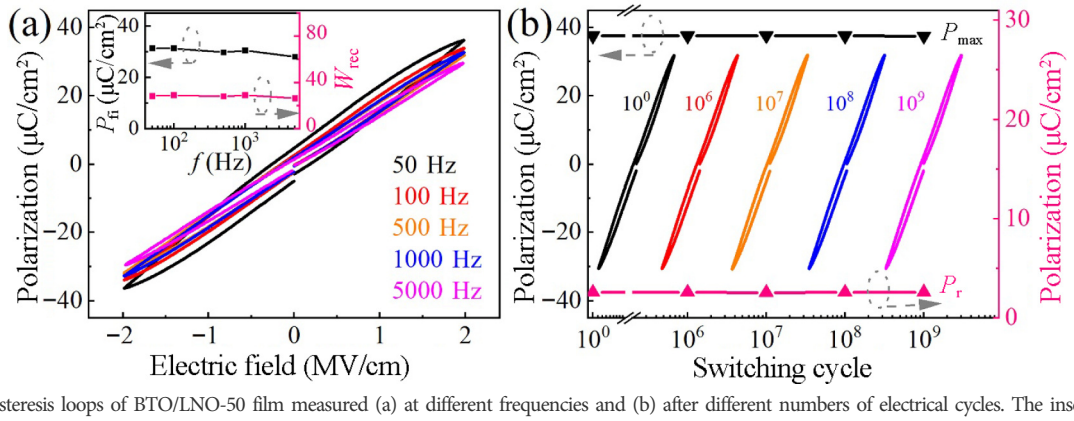

Fig. 8 *P*–*E* hysteresis loops of BTO/LNO-50 film measured (a) at different frequencies and (b) after different numbers of electrical cycles. The inset in (a) shows frequency dependence of field-induced polarization (P_{fi}) and recyclable energy density (W_{rec}).

Table 4 Comparison with leading $BaTiO_3$ dielectric films for capacitive energy storage in terms of processing temperature, field-induced polarization (P_{fi}), recyclable energy density (W_{rec}), and energy efficiency (η)

Deposition temperature (°C)	Measuring electric field, E (MV/cm)	P_{fi} (μC/cm²)	W_{rec} (J/cm³)	η	Ref.
700	2.6*	31.7	35.4	71.0%	[56]
650	2.6*	25.5	28.6	76.0%	[57]
500	2*	24.8	33.8	61.0%	[58]
500	3.14*	62.6	81.0	69.6%	[45]
500	4	78.5	132.8	65.5%	[46]
400	4	30.8	56.7	92.2%	[50]
350	4	36.6	63.9	79.5%	[43]
350	4	47.6	82.1	86.3%	[47]
200	4	55.8	94.7	78.2%	This work

Note: * These electric fields are the maximum ones reported for the corresponding films.

deposited ferroelectric films. A large field-induced polarization (~55.8 μC/cm²@4 MV/cm) and an excellent energy storage performance (W_{rec} ≈ 94.7 J/cm³, η ≈ 78.2%@4 MV/cm) were achieved in the $BaTiO_3$ films with an optimized thickness of the buffer layer $LaNiO_3$ (~50 nm). Proper crystallization with a small grain size, together with a grain population dominated by highly polarizable (111) and (110) grains, are the key factors for the charge/energy storage performances of the BTO/LNO-50 film. This work provides an integration-friendly sputter-deposition route (200 °C for the ferroelectric film and 300 °C for the entire process, including Pt/Ti deposition) for the growth of high-quality $BaTiO_3$ films on Si, which is a promising material candidate for a variety of microelectronic technologies, especially those aimed at energy buffering, charge or energy storage and supply. The strategy we proposed in this work also applies to other dielectrics for integrated applications.

Acknowledgements

This work was supported by the Natural Science Foundation of Shandong Province (Nos. ZR2022ZD39, ZR2022QB138, ZR2020QE042, ZR2023QE138, ZR2022QB119, and ZR2022ME031), the National Natural Science Foundation of China (Nos. 92463306 and 52002192), the Innovation Capacity Improvement Project of Small and Medium-sized Technology-based Enterprises of Shandong Province (No. 2021TSGC1087), the Jinan City Science and Technology Bureau (No. 2021GXRC055), the Science, Education and Industry Integration Pilot Projects of Qilu University of Technology (Shandong Academy of Sciences) (Nos. 2022GH018, 2023PX062, and 2023PX041), the Seed Funding for Top Talents at Qilu University of Technology (Shandong Academy of Sciences), and the Excellent Teaching Team Training Plan Project of Qilu University of Technology, the Education Department of Hunan Province/Xiangtan University (No. KZ0807969).

Declaration of competing interest

The authors have no competing interests to declare that are relevant to the content of this article. The author Jun Ouyang is the Editorial Committee member of this journal.

References

[1] Niu X, Jian XD, Gong WP, *et al.* Field-driven merging of polarizations and enhanced electrocaloric effect in $BaTiO_3$-based lead-free ceramics. *J Adv Ceram* 2022, **11**: 1777–1788.
[2] Song CQ, Zheng FF, Zhang Y, *et al.* Dielectric ultracapacitors based on columnar nano-grained ferroelectric oxide films with gradient phases along the growth direction. *J Adv Ceram* 2024, **13**: 1072–1079.
[3] Acosta M, Novak N, Rojas V, *et al.* $BaTiO_3$-based piezoelectrics: Fundamentals, current status, and perspectives. *Appl Phys Rev* 2017, **4**: 041305.
[4] Peddigari M, Wang B, Wang R, *et al.* Giant energy density via mechanically tailored relaxor ferroelectric behavior of PZT thick film. *Adv Mater* 2023, **35**: 2302554.
[5] Muralt P, Kohli M, Maeder T, *et al.* Fabrication and characterization of PZT thin-film vibrators for micromotors. *Sens Actuat A—Phys* 1995, **48**: 157–165.
[6] Dalakoti A, Bandyopadhyay A, Bose S. Effect of Zn, Sr, and Y addition on electrical properties of PZT thin films. *J Am Ceram Soc* 2006, **89**: 1140–1143.
[7] Zhang M, Deng CY. Orientation and electrode configuration dependence on ferroelectric, dielectric properties of $BaTiO_3$ thin films. *Ceram Int* 2019, **45**: 22716–22722.
[8] Hao YN, Wang XH, Bi K, *et al.* Significantly enhanced energy storage performance promoted by ultimate sized ferroelectric $BaTiO_3$ fillers in nanocomposite films. *Nano Energy* 2017, **31**: 49–56.
[9] Qian WQ, Wu HT, Yang Y. Ferroelectric $BaTiO_3$ based multi-effects coupled materials and devices. *Adv Electron Mater* 2022, **8**: 2200190.
[10] Scott JF, Paz de Araujo CA. Ferroelectric memories. *Science* 1989, **246**: 1400–1405.
[11] Mikolajick T, Schroeder U, Slesazeck S. The past, the present, and the future of ferroelectric memories. *IEEE T Electron Dev* 2020, **67**: 1434–1443.
[12] Liu XP, Wei CS, Sun TY, *et al.* A $BaTiO_3$-based flexible ferroelectric capacitor for non-volatile memories. *J Materiomics* 2025, **11**: 100870.
[13] Kanno I. Fundamentals of piezoelectric thin films for microelectromechanical systems. In: *Nanostructures in Ferroelectric Films for Energy Applications*. Amsterdam (the Netherlands): Elsevier, 2019: 237–255.
[14] Huang Y, Shu L, Hu FD, *et al.* Implementing (K,Na)NbO_3-based lead-free ferroelectric films to piezoelectric micromachined ultrasonic transducers. *Nano Energy* 2022, **103**: 107761.
[15] Park KI, Xu S, Liu Y, *et al.* Piezoelectric $BaTiO_3$ thin film nanogenerator on plastic substrates. *Nano Lett* 2010, **10**: 4939–4943.
[16] Hyun SD, Park HW, Park MH, *et al.* Field-induced ferroelectric $Hf_{1-x}Zr_xO_2$ thin films for high-*k* dynamic random access memory. *Adv Elect Mater* 2020, **6**: 2000631.
[17] Wang K, Liu C, Zhang Y, *et al.* Pushing the high-*k* scalability limit with a superparaelectric gate layer. *J Adv Ceram* 2024, **13**: 539–547.
[18] Cheng HB, Zhai X, Ouyang J, *et al.* Achieving a high energy storage density in Ag(Nb,Ta)O_3 antiferroelectric films via nanograin engineering. *J Adv Ceram* 2023, **12**: 196–206.
[19] Liu JP, Wang Y, Zhu HF, *et al.* Synergically improved energy storage performance and stability in sol–gel processed $BaTiO_3$/(Pb,La,Ca)TiO_3/$BaTiO_3$ tri-layer films with a crystalline engineered sandwich structure. *J Adv Ceram* 2023, **12**: 2300–2314.
[20] Tian TF, Chen FL, Zhang LB, *et al.* Advances in energy storage of $AgNbO_3$-based antiferroelectric ceramics. *Adv Ceram* 2023, **44**: 153–172. (in Chinese)
[21] Wang HX, Zhao PY, Chen LL, *et al.* Energy storage properties of $0.87BaTiO_3$–$0.13Bi(Zn_{2/3}(Nb_{0.85}Ta_{0.15})_{1/3})O_3$ multilayer ceramic capacitors with thin dielectric layers. *J Adv Ceram* 2020, **9**: 292–302.
[22] Yao FZ, Yuan QB, Wang Q, *et al.* Multiscale structural engineering of dielectric ceramics for energy storage applications: From bulk to thin films. *Nanoscale* 2020, **12**: 17165–17184.
[23] Li Q, Yao FZ, Liu Y, *et al.* High-temperature dielectric materials for electrical energy storage. *Annu Rev Mater Res* 2018, **48**: 219–243.
[24] Chen MJ, Afridi KK, Perreault DJ. Stacked switched capacitor energy buffer architecture. *IEEE Trans Power Electron* 2013, **28**: 5183–5195.
[25] Van Tassell B, Yang S, Le CR, *et al.* Metacapacitors: Printed thin film,

flexible capacitors for power conversion applications. *IEEE Trans Power Electron* 2016, **31**: 2695–2708.
[26] Khan AI, Keshavarzi A, Datta S. The future of ferroelectric field-effect transistor technology. *Nat Electron* 2020, **3**: 588–597.
[27] Mikolajick T, Slesazeck S, Mulaosmanovic H, *et al.* Next generation ferroelectric materials for semiconductor process integration and their applications. *J Appl Phys* 2021, **129**: 100901.
[28] Baek S, Yoo HH, Ju JH, *et al.* Ferroelectric field-effect-transistor integrated with ferroelectrics heterostructure. *Adv Sci* 2022, **9**: 2200566.
[29] Liang ZS, Ma CR, Shen LK, *et al.* Flexible lead-free oxide film capacitors with ultrahigh energy storage performances in extremely wide operating temperature. *Nano Energy* 2019, **57**: 519–527.
[30] Luo SB, Yu JY, Yu SH, *et al.* Significantly enhanced electrostatic energy storage performance of flexible polymer composites by introducing highly insulating-ferroelectric microhybrids as fillers. *Adv Energy Mater* 2019, **9**: 1803204.
[31] Mallick S, Ahmad Z, Qadir KW, *et al.* Effect of $BaTiO_3$ on the sensing properties of PVDF composite-based capacitive humidity sensors. *Ceram Int* 2020, **46**: 2949–2953.
[32] Huang HM, Li HY, Wang XX, *et al.* Detecting low concentration of H_2S gas by $BaTiO_3$ nanoparticle-based sensors. *Sens Actuat B—Chem* 2017, **238**: 16–23.
[33] Chandran R, Sreekala CO, Menon SK. $BaTiO_3/V_2O_5$ composite based cylindrical dielectric resonator antenna for X-band applications. *Mater Today Proc* 2020, **33**: 1367–1370.
[34] Li C, Zhu M, Ji P, *et al.* In-fiber $BaTiO_3$ microsphere resonator for high-sensitivity temperature measurement. *Micromachines* 2021, **12**: 318.
[35] Chang LH, Anderson WA. Stability of $BaTiO_3$ thin films on Si. *Appl Surf Sci* 1996, **92**: 52–56.
[36] Law TW, Liu CK, Cheng PL, *et al.* Novel low temperature $BaTiO_3$ film capacitors. In: Proceedings of the 52nd Electronic Components and Technology Conference, San Diego, USA, 2002: 1714–1717.
[37] Wei ZQ, Noda M, Okuyama M. A very low-temperature growth of $BaTiO_3$ thin film by hydrothermal treatment following sol–gel coating at 200 degree Celsius. *Integr Ferroelectr* 2003, **52**: 111–118.
[38] Nam SM. Low temperature fabrication of $BaTiO_3$ thick films by aerosol deposition method and their electric properties. *Trans Mater Res Soc Jpn* 2004, **29**: 1215–1218.
[39] Zhu J, Liang Z, Li YR, *et al.* Epitaxial growth of $BaTiO_3$ thin films at a low temperature under 300 °C with temperature-controlled $BaTiO_3$ buffer layer. *J Cryst Growth* 2006, **294**: 236–242.
[40] Xu JB, Shen B, Zhai JW. Structure, dielectric and ferroelectric properties of highly (100)-oriented $BaTiO_3$ grown under low-temperature conditions. *Appl Surf Sci* 2009, **255**: 5922–5925.
[41] Zhang W, Hu FR, Zhang H, *et al.* Investigation of the electrical properties of RF sputtered $BaTiO_3$ films grown on various substrates. *Mater Res Bull* 2017, **95**: 23–29.
[42] Gao YQ, Yuan ML, Sun X, *et al. In situ* preparation of high quality $BaTiO_3$ dielectric films on Si at 350–500 °C. *J Mater Sci—Mater El* 2017, **28**: 337–343.
[43] Zhao YY, Ouyang J, Wang K, *et al.* Achieving an ultra-high capacitive energy density in ferroelectric films consisting of superfine columnar nanograins. *Energy Storage Mater* 2021, **39**: 81–88.
[44] Yuan ML, Zhang W, Wang XY, *et al. In situ* preparation of high dielectric constant, low-loss ferroelectric $BaTiO_3$ films on Si at 500 °C. *Appl Surf Sci* 2013, **270**: 319–323.
[45] Ouyang J, Teng XM, Yuan ML, *et al.* Grain engineering of high energy density $BaTiO_3$ thick films integrated on Si. *Microstructures* 2023, **3**: 2023027.
[46] Ouyang J, Xue YX, Song CQ, *et al.* Simultaneously achieving high energy density and responsivity in submicron $BaTiO_3$ film capacitors integrated on Si. *J Adv Ceram* 2024, **13**: 198–206.
[47] Zhu HF, Zhao YY, Ouyang J, *et al.* Achieving a record-high capacitive energy density on Si with columnar nanograined ferroelectric films. *ACS Appl Mater Inter* 2022, **14**: 7805–7813.
[48] Ianculescu A, Despax B, Bley V, *et al.* Structure–properties correlations for barium titanate thin films obtained by rf-sputtering. *J Eur Ceram Soc* 2007, **27**: 1129–1135.
[49] Zhang W, Cheng HB, Yang Q, *et al.* Crystallographic orientation dependent dielectric properties of epitaxial $BaTiO_3$ thin films. *Ceram Int* 2016, **42**: 4400–4405.
[50] Wang K, Zhang Y, Wang SX, *et al.* High energy performance ferroelectric $(Ba,Sr)(Zr,Ti)O_3$ film capacitors integrated on Si at 400 °C. *ACS Appl Mater Inter* 2021, **13**: 22717–22727.
[51] Wang K, Ouyang J, Wuttig M, *et al.* Superparaelectric $(Ba_{0.95},Sr_{0.05})(Zr_{0.2},Ti_{0.8})O_3$ ultracapacitors. *Adv Energy Mater* 2020, **10**: 2001778.
[52] Zhao YY, Ouyang J. Columnar nanograined $BaTiO_3$ ferroelectric thin films integrated on Si with a sizable dielectric tunability. *J Inorg Mater* 2022, **37**: 596.
[53] Yang CH, Feng C, Lv PP, *et al.* Coexistence of giant positive and large negative electrocaloric effects in lead-free ferroelectric thin film for continuous solid-state refrigeration. *Nano Energy* 2021, **88**: 106222.
[54] Chen J, Wang YF, Yuan QB, *et al.* Multilayered ferroelectric polymer films incorporating low-dielectric-constant components for concurrent enhancement of energy density and charge–discharge efficiency. *Nano Energy* 2018, **54**: 288–296.
[55] Chen MS, Wu TB, Wu JM. Effect of textured $LaNiO_3$ electrode on the fatigue improvement of $Pb(Zr_{0.53}Ti_{0.47})O_3$ thin films. *Appl Phys Lett* 1996, **68**: 1430–1432.
[56] Zhang W, Gao YQ, Kang LM, *et al.* Space-charge dominated epitaxial $BaTiO_3$ heterostructures. *Acta Mater* 2015, **85**: 207–215.
[57] Zhu HF, Liu ML, Zhang YX, *et al.* Increasing energy storage capabilities of space-charge dominated ferroelectric thin films using interlayer coupling. *Acta Mater* 2017, **122**: 252–258.
[58] Liu ML, Zhu HF, Zhang YX, *et al.* Energy storage characteristics of $BiFeO_3/BaTiO_3$ bi-layers integrated on Si. *Materials* 2016, **9**: 935.